

Spontaneous Anomalous Hall Effect in Two-Dimensional Altermagnets

Sajjan Sheoran and Pratibha Dev

Department of Physics and Astronomy, Howard University, Washington D.C., USA

The anomalous Hall effect (AHE) is an efficient tool for detecting the Néel vector in collinear compensated magnets with spin-split bands, known as altermagnets (AMs). Here, we establish design principles for obtaining non-zero anomalous Hall conductivity in the recently proposed two-dimensional (2D) AMs using spin and magnetic group symmetry analysis. We show that only two of the seven nontrivial spin layer groups exhibit an unconventional in-plane AHE in which the Néel vector lies within the plane of the Hall current. Through first-principles simulations on bilayers of MnPSe₃ and MnSe, we demonstrate the validity of our group theoretic framework for obtaining AHE with *d* and *i*-wave altermagnetic orders, depending on the stacking of the bilayers. We find that the spin group symmetry is successful in determining the linear and cubic dependence of anomalous Hall conductivity in Néel vector space, although AHE is a relativistic effect. This work shows that the AHE in 2D AMs can probe the altermagnetic order and Néel vector reversal, thereby facilitating the miniaturization of altermagnetic spintronics.

I. INTRODUCTION

Altermagnetism (AM) has emerged as a novel class of collinear magnetism characterized by time-reversal symmetry (T) breaking in momentum space along with compensated magnetic order in real space [1–5]. Unlike conventional antiferromagnets (AFMs), where the opposite spin sublattices are connected by the inversion (P) and/or translation (τ) operations, in AMs they are connected by mirror-rotation symmetries. Hence, AMs show eV-scale nonrelativistic spin splittings [3], leading to highly spin-polarized currents, which are characteristic of ferromagnets (FMs). Since there is no net magnetization, AMs also show ultrafast switching dynamics and resilience towards stray fields, similar to that shown by AFMs [6–9]. This combination of properties of both FMs and AFMs in a single material makes AMs interesting not only for fundamental research, but also for spintronics-based applications by allowing for facile control and detection of spin states using different means, including electric or optical fields. Broken T -symmetry effects in AMs are experimentally detected through angle-resolved photoemission spectroscopy [10, 11], spin-to-charge interconversion [12, 13], and the anomalous Hall effect (AHE) [14]. To date, the experimental observation of altermagnetic effects is still limited to three-dimensional (3D) materials, i.e., MnTe [15], Mn₅Si₃ [16], CrSb [17], and RuO₂ [12].

The discovery of magnetic ordering in atomically thin materials opens up new possibilities for miniaturizing devices to the two-dimensional (2D) limit. However, achieving AM in 2D systems is difficult due to additional symmetry constraints. In 2D layers, the electronic bands are dispersionless along the out-of-plane direction [18–21]. As a result, in the 2D limit, the two-fold rotation along the z -axis (C_2^z) and horizontal mirror (M_z) symmetry transform $\mathbf{k} = (k_x, k_y)$ like P and τ , respectively. Therefore, for altermagnetism to emerge, the opposite spin sublattices must not be connected by M_z and/or C_2^z [19]. In spite of these exacting requirements, AM in 2D materi-

als was predicted theoretically using a high-throughput computational approach (RuF₄, FeBr₃ [22, 23]), bilayer stackings (CrSBr, MnBi₂Te₄ [18, 20]) and twisting bilayers [21, 24, 25]. The nonrelativistic understanding of 2D altermagnetism was recently established in Refs. [18–25]. However, unlike 3D bulk AMs, a comprehensive analysis of the magnetotransport effects (such as anomalous Hall and anomalous Nernst effects), and novel Néel vector detection methods for 2D AMs is still lacking.

Our work based on symmetry analysis and first-principles simulations elucidates the stringent symmetry requirement for observing AHE in the 2D AMs. We show an unconventional periodic dependence of AHE on the Néel-vector space, where the Néel vector lies in the plane of the Hall current. This is in contrast to the conventional FM-like Hall response, where Hall current is perpendicular to the magnetization [26, 27]. By performing density functional theory (DFT) simulations on bilayers of MnPSe₃ and MnSe, which are PT -symmetric as monolayers, we achieved *d*- and *i*-wave altermagnetism with an in-plane anomalous Hall response as large as for the well-known bulk AMs—MnTe [15, 28] and Mn₅Si₃ [16, 29]. Furthermore, we reveal the unique relationship of the AHE with the spin group symmetries and nonrelativistic spin-degenerate nodal lines. Moreover, the in-plane AHE is shown to be an efficient tool to probe the altermagnetic order and 180° Néel vector reversal in 2D AMs.

II. CALCULATION METHODS

DFT calculations have been carried out using the projector-augmented wave method [30], as implemented in the VASP package [31]. The Perdew-Burke-Ernzerhof (PBE) [32] functional within the generalized-gradient approximation, along with a Hubbard U correction, are employed to accurately describe electronic interactions. Following Refs. [33, 34], an effective U value of 3.0 eV was applied to the Mn-*d* orbitals using the approach of Dudarev *et al.* [35]. The Grimme-D3 scheme was used to account for the vdW interactions [36].

TABLE I. Symmetry constraints on the components of the anomalous Hall conductivity tensor imposed by the magnetic point group operations. \checkmark and \times denotes symmetry allowed and forbidden components, respectively. The z (x) denotes the out-of-plane (in-plane) direction.

	P	C_n^z	C_n^x	M_z	M_x	$S_{4,6}^z$	$S_{4,6}^x$	T	PT	TC_2^z	TC_2^x	TM_z	TM_x	$TC_{3,4,6}^{x,z}$	$TS_{4,6}^{x,z}$
σ_{xy}	\checkmark	\checkmark	\times	\checkmark	\times	\checkmark	\times	\times	\times	\times	\checkmark	\times	\checkmark	\times	\times
σ_{xz}	\checkmark	\times	\times	\times	\times	\times	\times	\times	\times	\checkmark	\checkmark	\checkmark	\checkmark	\times	\times
σ_{yz}	\checkmark	\times	\checkmark	\times	\checkmark	\times	\checkmark	\times	\times	\checkmark	\times	\checkmark	\times	\times	\times

The AHE can be described by an order parameter called the Hall vector (σ_H), with the anomalous Hall current density given by $\mathbf{J} = \sigma_H \times \mathbf{E}$, where \mathbf{E} is the electric field. The Hall vector is defined as: $\sigma_H = (\sigma_{zy}, \sigma_{xz}, \sigma_{yx})$ [37], with $\sigma_{\alpha\beta}$ for $\alpha \neq \beta$ being the antisymmetric components of the conductivity tensor. At the microscopic level, the intrinsic contribution to anomalous Hall conductivity (AHC) is expressed as

$$\sigma_{\alpha\beta} = -\epsilon_{\alpha\beta\gamma} \frac{e^2}{\hbar} \int \frac{d\mathbf{k}}{(2\pi)^3} \sum_n f(\mathcal{E}_{n,\mathbf{k}}) \Omega_\gamma(n, \mathbf{k}) \quad (1)$$

where $\epsilon_{\alpha\beta\gamma}$ is Levi-Civita symbol. $\mathcal{E}_{n,\mathbf{k}}$ and Ω_γ are the energy eigenvalue and Berry curvature, respectively, of the band with quantum number n . $f(\mathcal{E}_{n,\mathbf{k}})$ is the Fermi-Dirac distribution function. At zero temperature, the summation in Eq. 1 reduces to a sum over occupied bands. To simulate AHC within DFT, we constructed a tight-binding Hamiltonian from maximally localized Wannier functions, which were obtained through Wannier90 [38]. Wannier interpolation of Berry curvature and AHC were postprocessed using the “pruned FFT”-based WannierBerri [39] package. Note that rapid variations of Berry curvature are taken into account by integrating the Brillouin Zone on a dense k -mesh of $125 \times 125 \times 1$ and with recursive adaptive mesh refinement. We conducted symmetry analysis using Ref. [40], FINDSYM [41], Bilbao Crystallographic Server [42], MAGNDATA [43], and AMCHECK [44].

III. RESULTS AND DISCUSSION

A. Symmetry analysis for AHE in 2D AMs

Since AMs display spin-splitting of electronic structure without spin-orbit coupling (SOC), they are best characterized by spin group symmetries $[R_1 || R_2]$, where R_1 and R_2 symmetry operations act on the decoupled spin and real space, respectively [3, 45–47]. Just like in the case of AFMs, symmetry dictates a net zero magnetization in AMs. However, in AFMs, the spin-up and -down bands are degenerate. It is instructive to see which symmetries (in terms of spin group formalism) would result in a traditional AFM versus an AM. Collinear magnets, including AMs, always have spin-only symmetry $[\bar{C}_2 || T]$, where \bar{C}_2 is a two-fold rotation around the axis perpendicular to the collinear spins, followed by inversion in spin-space [45]. The $[\bar{C}_2 || T]$ transforms energy eigenstates

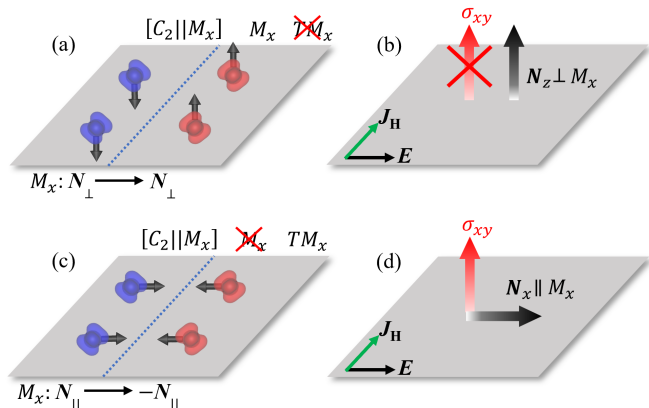


FIG. 1. Schematic diagram showing how symmetries determine the presence or absence of AHE in 2D altermagnets. In this example, the spin-group symmetry $[C_2 || M_x]$ connects the opposite spin-sublattices. (a) M_x symmetry is satisfied when the Néel vector (\mathbf{N}) is perpendicular to the direction of the mirror plane. Note that the direction of mirror plane refers to the direction normal to the mirror (here, x -direction). (b) M_x symmetry forbids the AHE (see Table I). (c) \mathbf{N} being parallel to the x -direction violates the M_x symmetry and (d) thus the AHE is symmetry allowed. Since \mathbf{N} , \mathbf{J}_H , and \mathbf{E} all lie in the same plane (here, the x - y plane), this is referred to as the in-plane AHE.

as $[\bar{C}_2 || T]E(s, \mathbf{k}) = E(s, -\mathbf{k})$, leading to even-parity spin splitting. The $[\bar{C}_2 || T][C_2 || P]$ and $[C_2 || \tau]$ transform the energy eigenstates from $E(s, \mathbf{k})$ to $E(-s, \mathbf{k})$, which lead to spin degeneracy at an arbitrary k -point. The C_2 operation is the two-fold rotation about an axis perpendicular to collinear spins in spin space and, for simplicity, can be interpreted as spin space inversion. Additionally, for the 2D case ($k_z = 0$), the spin-group symmetries $[C_2 || M_x]$ and $[C_2 || C_2^z]$ also lead to spin degeneracy (see Sec. I of Supplemental Material (SM) [48]). Overall, to obtain altermagnetism in 2D materials, opposite spin sublattices should not be connected by crystallographic P , τ , C_2^z , and M_x . However, there should exist at least one crystallographic symmetry connecting opposite spin sublattices to have symmetry-enforced net zero magnetization. The possible symmetry options are in-plane two-fold rotation (i.e., $[C_2 || C_2^x]$), vertical mirror plane (i.e., $[C_2 || M_x]$), and out-of-plane four-fold rotation ($[C_2 || C_4^z]$). The 2D AM case with $[C_2 || M_x]$ symmetry is highlighted in Fig. 1.

The symmetry analysis for the relativistic AHE requires the considerations of magnetic symmetry opera-

tions acting on coupled spin and real spaces. From the symmetry perspective, the Hall vector, $\boldsymbol{\sigma}_H$, transforms like a pseudovector, similar to magnetization. Therefore, the magnetic symmetry operations impose certain constraints on allowed components, σ_{ij} , of the system (see Table I and Sec. II of SM [48]). In particular, all components of the AHC tensor are symmetry forbidden if a material (2D or 3D) possesses either of the T , PT , $TC_{3,4,6}^{x,z}$, or $TS_{4,6}^{x,z}$ symmetries. Further constraints determining non-zero AHC are imposed by the 2D nature of the 2D AMs. As the Hall current is restricted to the plane of the 2D materials, the only component that is experimentally relevant is σ_{xy} (taking z as the out-of-plane axis). Hence, the presence of C_n^x , M_x , TM_z , and TC_2^z symmetries suppresses AHE in 2D materials as these symmetries result in zero σ_{xy} [see Table I]. Overall, our symmetry analysis shows that three of the following conditions must be simultaneously satisfied to obtain a 2D AM with AHE: (i) absence of $[C_2||P]$, $[C_2||\tau]$, $[C_2||M_z]$, and $[C_2||C_2^z]$ spin group symmetries that will otherwise indicate that we have a conventional AFM, (ii) presence of at least one of $[C_2||C_2^x]$, $[C_2||M_x]$, and $[C_2||C_4^z]$ spin group symmetries, ensuring altermagnetism, and (iii) absence of T , PT , $TC_{3,4,6}^{x,z}$, $TS_{4,6}^{x,z}$, C_n^x , M_x , TM_z , and TC_2^z magnetic symmetries, which ensures non-zero σ_{xy} . These conditions for obtaining 2D AMs with AHE are partially related. For example, $[C_2||P]$ and PT occur simultaneously in collinear magnets. These conditions make observing AHE difficult in 2D AMs, and have largely remained unexplored.

The magnetic symmetries depend on the Néel vector orientation with respect to the crystal symmetry. The Néel vector serves as an order parameter for AFMs and offers a robust nonvolatile approach to modifying magnetic symmetries [49]. Since, AMs also have net zero magnetization, the Néel vector could serve as a natural way to modify AHE. For example, consider the case of a 2D AM with $[C_2||M_x]$ symmetry, where opposite spin sublattices are connected through a vertical mirror plane (see Fig. 1). When the Néel vector is perpendicular to the x -direction, the magnetic point group of the AM will contain M_x , leading to vanishing σ_{xy} [Figs. 1(a) and 1(b)]. However, aligning the Néel vector along the x -direction will lead to the breaking of the M_x symmetry [Fig. 1(c)]. Hence, the presence of the Néel vector along the x -direction will allow σ_{xy} [Fig. 1(d)]. It is worth mentioning that M_x and C_2^x impose the same condition on σ_{xy} [see Table I]. Therefore, the presence of $[C_2||C_2^x]$ will allow (forbid) σ_{xy} when the Néel vector is parallel (perpendicular) to x direction. Following the same approach, we have classified the 2D AMs based on whether the AHE is allowed for the different Néel vector orientations, spin-momentum coupling and their nontrivial spin layer group (SLG) (see Table II and Sec. III of SM [48]). Interestingly, d -wave AMs with nontrivial SLG $2^2/2^2m$ and i -wave AMs with nontrivial SLG 1^32^2m allows for an in-plane AHE, where \mathbf{N} , \mathbf{J}_H , and \mathbf{E} lie in the $x-y$ plane. Additionally, AMs with nontrivial SLGs $2^2m^2m^1m$, $2^4/1^4m$,

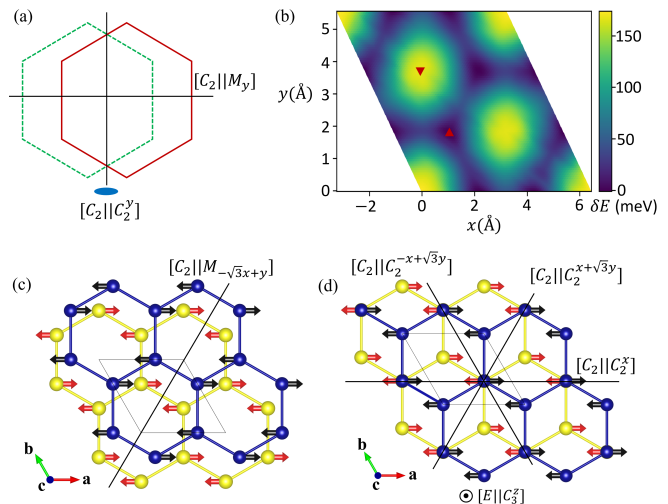


FIG. 2. Generation of AM through bilayer stackings. (a) The upper layer is obtained by taking the horizontal mirror reflection of the lower layer followed by in-plane translation. The bilayer stacking may have $[C_2||M_y]$ and $[C_2||C_2^y]$ -like spin group symmetries depending on the shifting vector and the constituent monolayer. (b) The energy distribution of the bilayer MnPSe_3 as a function of the shifting of the upper layer. (c) and (d) highlights the two high-symmetry stackings obtained by shifting the upper layer by $\frac{1}{3}\mathbf{a} + \frac{1}{3}\mathbf{b}$ (d - MnPSe_3) and $\frac{1}{3}\mathbf{a} + \frac{2}{3}\mathbf{b}$ (i - MnPSe_3), respectively, with representative Néel vector along x -direction. The blue and yellow spheres denote the Mn atoms from the top and bottom layers, respectively. We have omitted the P and Se atoms for clear illustration (see Fig. S2 in the SM [48] for complete structure). The position of structures in (c) and (d) are also highlighted in potential energy surfaces in (b) with up- and down-triangle, respectively. The spin group symmetry operations are also indicated for each case.

$2^4/1^4m^2m^1m$, $1^4/1^4m^2m^2m$, and $1^6/1^6m^2m^2m$ do not show an in-plane AHE due to the presence of TC_2^z symmetry. In accordance to symmetry analysis, σ_{xy} is always forbidden for 2D AMs when Néel vector points along the z -direction.

B. Bilayer AMs as prototypical candidates

We exemplify the symmetry predictions of AHE in the 2D AMs using DFT simulations. For this, we chose the prototypical experimentally-synthesized AFM materials – MnPSe_3 [52–54] and MnSe [33, 55–57] monolayers. In what follows, we provide detailed results for MnPSe_3 , while details of our calculations for MnSe are included in the supplemental material [48]. Both MnPSe_3 and MnSe monolayers form a large class of 2D materials with G and A type AFM order, respectively, and a Néel transition temperature of ~ 75 K [55, 58]. The PT symmetry in MnPSe_3 and MnSe monolayers enforces spin-degeneracy and forbids the AHE effect (see Sec. IV of SM [48]). To obtain AM, we break PT symmetry of

TABLE II. AHE in 2D AMs with different nontrivial spin-Layer group (SLG) symmetry. The superscripts 1 and 2 denote symmetry operations connecting atoms with the same and opposite spin magnetizations, respectively. Spin-momentum coupling is categorized based on the number of spin-degenerate nodal lines in the band dispersion. Specifically, d -, g -, and i -wave AMs exhibit 2, 4, and 6 spin-degenerate nodal lines passing through the Γ point, respectively, in the (k_x-k_y) momentum space. The nontrivial spin group symmetry operations are highlighted for each case. Note that the spin group operations $[E||E]$ and $[E||P]$ are excluded as they impose no restrictions on the AHC. Symmetry-invariant terms describe the functional dependence of the AHC σ_{xy} on the Néel vector components (N_x, N_y, N_z) . The table also specifies whether σ_{xy} is allowed when the Néel vector is perpendicular or parallel to the out-of-plane direction (z). For forbidden cases, the relevant magnetic symmetry responsible is also indicated. Symmetry invariants up to cubic in N_i are included. Note that symmetry invariants may encompass higher-order terms, though their contributions are expected to be weak. Additionally, examples of well-known 2D AMs belonging to different SLGs are also tabulated. Entries marked with $[\star]$ denote examples from this work.

Nontrivial SLG	Spin-momentum coupling	Nontrivial spin group operations	Symmetry-allowed σ_{xy} terms	σ_{xy}		Examples
				$N \perp z$	$N \parallel z$	
${}^2_2/{}^2m$	d -wave	$[C_2 C_2^x]$	$N_x^{1,3}, N_x N_y^a N_z^b$ ($a+b=2$)	\checkmark	$\times (C_2^z)$	RuF ₄ [23], d -MnPSe ₃ $[\star]$
${}^2m^2m^1m$	d -wave	$[C_2 C_2^x], [E C_2^z]$	$N_x N_y N_z$	$\times (TC_2^z)$	$\times (C_2^z)$	MnTeMoO ₆ [19]
${}^2_4/{}^1m$	d -wave	$[C_2 C_4^z], [E C_2^z]$	$N_x^2 N_z - N_y^2 N_z, N_x N_y N_z$	$\times (TC_2^z)$	$\times (C_2^z)$	
${}^2_4/{}^1m^2m^1m$	d -wave	$[C_2 C_4^z], [E C_2^z, C_2^x]$	$N_x^2 N_z - N_y^2 N_z$	$\times (TC_2^z)$	$\times (C_2^z)$	VSe ₂ O [50], CrO[51]
${}^1_4/{}^1m^2m^2m$	g -wave	$[C_2 C_2^x], [E C_4^z, C_2^x]$	—	$\times (TC_2^z)$	$\times (C_2^z)$	VP ₂ H ₈ (NO ₄) ₂ [19]
${}^1_3{}^2m$	i -wave	$[C_2 C_2^x], [E C_3^z]$	$N_x^3 - 3N_x N_y^2$	\checkmark	$\times (C_2^z)$	i -MnPSe ₃ $[\star]$
${}^1_6/{}^1m^2m^2m$	i -wave	$[C_2 C_2^x], [E C_3^z, C_2^z]$	—	$\times (TC_2^z)$	$\times (C_2^z)$	

the monolayer MnPSe₃ and MnSe by using the bilayer stacking approach [see Fig 2(a)] [18]. We created different bilayer stacking by first taking the top layer to be the mirror reflection of the lower layer, followed by the translation of the upper layer in the basal plane. We have also used two different magnetic configurations with intralayer AFM, namely, $M\uparrow\uparrow\downarrow\downarrow$ and $M\uparrow\downarrow\downarrow\uparrow$ (the four arrows denote the magnetization directions of Mn atoms, with first two arrows being used for the lower layer and the last two arrows for the upper layer). The configurations $M\uparrow\uparrow\downarrow\downarrow$ and $M\uparrow\downarrow\downarrow\uparrow$ are almost degenerate (differing by around 0.22 meV), signifying the weak interlayer exchange interaction. Further, DFT calculations were performed for potential energy surfaces of various high symmetry stackings [see Fig 2(b) for MnPSe₃]. There are 6 degenerate lowest-energy configurations. These stackings are equivalent by symmetry and are obtained through translation of the upper layer by $\frac{1}{3}\mathbf{a}$, $\frac{1}{3}\mathbf{b}$, $\frac{2}{3}\mathbf{a}$, $\frac{2}{3}\mathbf{b}$, $\frac{1}{3}\mathbf{a} + \frac{1}{3}\mathbf{b}$, and $\frac{2}{3}\mathbf{a} + \frac{2}{3}\mathbf{b}$. Similarly, three high-energy stacking configurations, obtained through translation of the upper layer by $\mathbf{0}$, $\frac{1}{3}\mathbf{a} + \frac{2}{3}\mathbf{b}$, and $\frac{2}{3}\mathbf{a} + \frac{1}{3}\mathbf{b}$, are degenerate. Therefore, we take representative cases of bilayer MnPSe₃ obtained through $\frac{1}{3}\mathbf{a} + \frac{1}{3}\mathbf{b}$ [see Fig 2(c)] and $\frac{1}{3}\mathbf{a} + \frac{2}{3}\mathbf{b}$ [see Fig 2(d)] and we name those stackings as d -MnPSe₃ and i -MnPSe₃, respectively. The rationale behind this unconventional nomenclature is elaborated in the following paragraph. The most stable Néel ordering is $M\uparrow\uparrow\downarrow\downarrow$ and $M\uparrow\downarrow\downarrow\uparrow$ for d -MnPSe₃ and i -MnPSe₃, respectively, and therefore used in our simulations. Although, i -MnPSe₃ is not the most stable bilayer stacking [see Fig 2(d)], it serves a qualitative analysis of AHE in the materials sharing structural similarity. For instance, twisted bilayers (tb) of hexagonal materials (such as tb-NiCl₂ [21], tb-MnBi₂Te₄ [24], and tb-MnPSe₃ [25]), have the same nonmagnetic and magnetic point group as of i -MnPSe₃. However, performing DFT+U+SOC simula-

tions on twisted bilayers are computationally formidable task owing to supercell size.

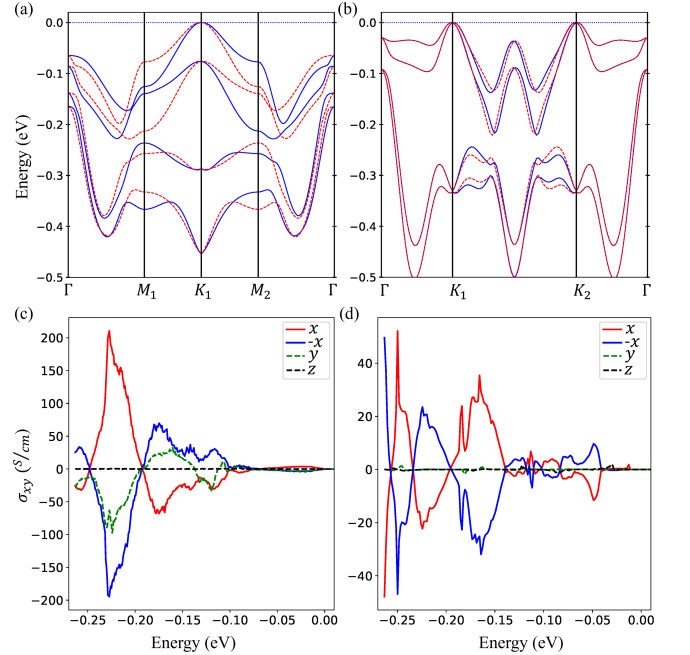


FIG. 3. Valence bands of (a) d -MnPSe₃ and (b) i -MnPSe₃ bilayer without inclusion of SOC. The red dashes and blue dots represent spin-up and spin-down bands, respectively. Anomalous Hall conductivity σ_{xy} of (c) d -MnPSe₃ and (d) i -MnPSe₃ as a function of Fermi energy for Néel vector pointing along different directions. The zero Fermi energy corresponds to valence band maximum.

We computed the electronic bands of d -MnPSe₃ and i -MnPSe₃ without SOC [see Figs. 3(a) and 3(b)]. The spin degeneracy in the energy bands can be explained through spin group symmetry operations [3]. The pres-

ence of $[C_2|O]$ symmetry leads to $[C_2|O]E(s, \mathbf{k}) = E(-s, O^{-1}\mathbf{k})$. Therefore, the bands are spin degenerate along the paths for which $O\mathbf{k} = \mathbf{k}$ or $O\mathbf{k} = \mathbf{k} + \mathbf{G}$, where \mathbf{G} is a reciprocal lattice vector. For d -MnPSe₃, the spin-up and spin-down states are degenerate for the bands along the directions perpendicular and parallel to the mirror plane due to $[C_2|M_{-\sqrt{3}x+y}]$ and $[\bar{C}_2|T][C_2|M_{-\sqrt{3}x+y}]$, respectively (see Sec. V of SM [48] for constant energy contours). AMs with two spin degenerate nodal lines are classified as d -wave AMs, and d -MnPSe₃ belong to that class [3]. Similarly, the energy bands in i -MnPSe₃ are spin degenerate along all possible high symmetry directions $\Gamma - M$, $\Gamma - K$, and $M - K$ due to presence of three $[C_2|C_2^x]$ -type spin group symmetries [Fig. 2(d)] and their combinations with spin-only symmetry $[\bar{C}_2|T]$. This results in the i -wave alternating magnetism in the i -MnPSe₃. Note that although bands are nondegenerate at the general k -point, the sum of spin splittings throughout the BZ, $\sum_{BZ} \mathcal{E}(s, \mathbf{k}) - \mathcal{E}(-s, \mathbf{k})$, is zero for each case [see Figs. 3(a) and 3(b)].

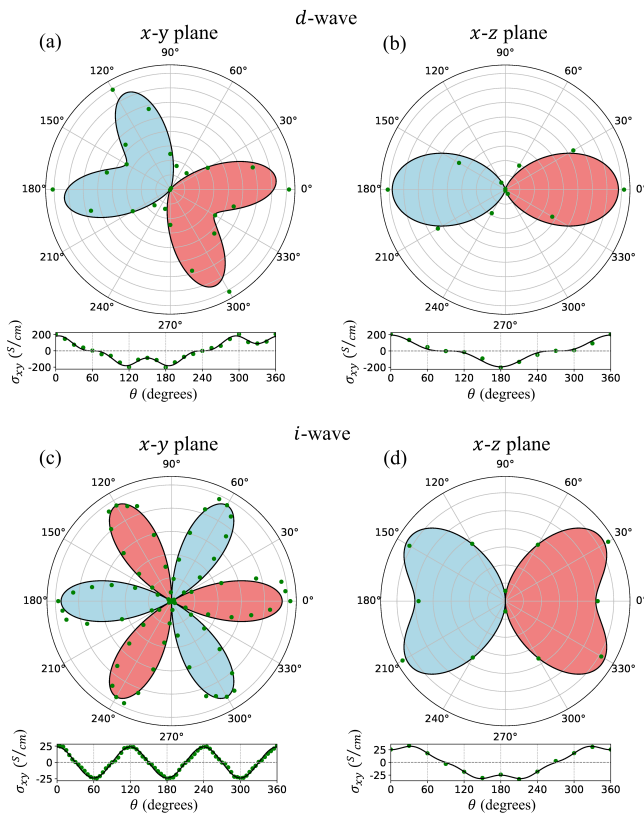


FIG. 4. The anomalous Hall conductivity (σ_{xy}) of d -MnPSe₃ with d -wave AM as a function of the Néel vector orientation in (a) x - y plane and (b) x - z plane at -0.23 eV. Similarly, (c) and (d) show the AHC for i -MnPSe₃ with i -wave AM at -0.17 eV. The regions with positive and negative σ_{xy} are highlighted with light red and light blue. The green dots represent the calculated DFT values while black curves are the fits using models in Eq. 2.

C. The AHC and Néel vector relationship

We calculate the AHC, σ_{xy} , as a function of the Fermi energy for d -MnPSe₃ and i -MnPSe₃ for different Néel vector, \mathbf{N} , orientations [Figs. 3(c) and 3(d)]. The σ_{xy} shows a strong dependence on the \mathbf{N} orientation and is absent when \mathbf{N} is along the z -direction. The anomalous Hall response is strongest for \mathbf{N} along the x -direction. The σ_{xy} for d -MnPSe₃ develops a strong peak of 202 S/cm around -0.23 eV, while σ_{xy} of i -MnPSe₃ develops a slightly weaker peak of 25 S/cm around -0.17 eV. Note that we observe a very sharp peak for i -MnPSe₃ around -0.25 eV and it may be difficult to achieve experimentally as it requires precise control of the Fermi energy. Interestingly, σ_{xy} is forbidden for \mathbf{N} aligned along the y -direction for i -MnPSe₃, while it shows an intermediate response for d -MnPSe₃. To understand this dependence of σ_{xy} on the Néel vector, we plot the anomalous Hall peaks for different \mathbf{N} orientations in the x - y and x - z planes (see Fig. 4). For the x - y plane, the AHE is absent in d -MnPSe₃ for the Néel vector along $60^\circ/240^\circ$ due to the presence of the vertical mirror $M_{-\sqrt{3}x+y}$ [Fig. 4(a)]. Similarly, the AHE is absent for i -MnPSe₃ when \mathbf{N} is perpendicular to any of the two-fold rotation symmetries ($30^\circ, 90^\circ, 150^\circ, 210^\circ, 270^\circ$, and 330°) [Fig. 4(c)]. When \mathbf{N} points in the z -direction, the AHE is forbidden due to presence of the $M_{-\sqrt{3}x+y}$ and C_2^x in d -MnPSe₃ and i -MnPSe₃, respectively [see Figs. 4(b) and 4(d)].

Furthermore, we understand the periodicity by writing the general functional form of σ_{xy} as $\sigma_{xy}(\mathbf{N}) = \sum_{m,n,r} \lambda_{mnr} N_x^m N_y^n N_z^r$, where m , n , and r are whole numbers. Some components of λ_{mnr} are forbidden due to symmetries. For instance, $m + n + r$ is never even as it would violate the Onsager reciprocity relation: $\sigma_{xy}(\mathbf{N}) = \sigma_{yx}(-\mathbf{N})$ [59]. We use the “method of invariants” [60] [$O\sigma_{xy}(O\mathbf{N}) = \sigma_{xy}(\mathbf{N})$] to obtain symmetry allowed components λ_{mnr} . For this, we treat \mathbf{N} as an extrinsic parameter instead of an intrinsic one [61, 62]. Recall that \mathbf{N} transforms like $\mathbf{N}' = \pm \text{Det}(O)D(O)\mathbf{N}$, where $D(O)$ and $\text{Det}(O)$ are the matrix representation and determinant of O . The $+$ ($-$) sign is taken if O exchanges the same (opposite) spin sublattices [see Figs 1(a) and 1(b)]. Table II summarizes the symmetry allowed profiles of $\sigma_{xy}(\mathbf{N})$ for 2D AMs with different spin group symmetry operations and nontrivial SLG (see also Sec. III of SM [48]). d -MnPSe₃ and i -MnPSe₃ have nontrivial SLG $2_2^2/m$ and $1_3^2/m$, respectively, and the $\sigma_{xy} - \mathbf{N}$ relationship can be expressed as

$$\begin{aligned} \sigma_{xy}^{2_2^2/m} &= \lambda_{100}N_x + \lambda_{300}N_x^3 + \lambda_{111}N_xN_yN_z + \lambda_{120}N_xN_y^2 \\ &\quad + \lambda_{102}N_xN_z^2 \\ \sigma_{xy}^{1_3^2/m} &= \lambda_{300}(N_x^3 - 3N_xN_y^2) + \lambda_{302}(N_x^3 - 3N_xN_y^2)N_z^2. \end{aligned} \quad (2)$$

In Fig. 4, we fit the calculated DFT values of σ_{xy} with the models in Eq. 2. Note that for d -MnPSe₃ the mirror plane is $M_{-\sqrt{3}x+y}$ and not M_x . Therefore, we have rotated the models accordingly while fitting. The mod-

els provide good agreement with the DFT results. However, the fit shows slight deviations from the DFT results, which may be due to the structural distortions relative to the ideal symmetric configurations, and/or because we have ignored the higher-order terms in Eq. 2. Note that the σ_{xy} of d -MnPSe₃ depends on linear and cubic terms in the Néel vector \mathbf{N} [Fig 4(a)], while i -MnPSe₃ exhibits a purely cubic dependence on \mathbf{N} [Fig 4(c)]. Consequently, the strength of AHC in i -MnPSe₃ is smaller than that in d -MnPSe₃, with three AHC-forbidden directions in the x - y plane of the Néel vector space.

The dependence of σ_{xy} on \mathbf{N} is derived for all 2D altermagnetic nontrivial SLGs in Table II. The AHE is forbidden for all g -wave 2D AMs due to the presence of $[E|C_4^z]$ symmetry, while the $[E|C_2^z, C_3^z]$ symmetries suppress the AHE in i -wave 2D AMs with the nontrivial SLG $^16/1m^2m^2m$. The presence of $[E|C_2^z]$, $[E|C_4^z]$, or $[C_2|C_4^z]$ leads to the presence of magnetic TC_2^z symmetry, which forbids the in-plane AHE. Most commonly, 2D magnets have an easy axis of magnetization that lies completely in-plane [34, 57] or out-of-plane [63, 64], and in such a scenario, the AHE can be observed for only $^22/2^2m$ and $^13^2m$ out of the seven nontrivial SLGs. Interestingly, the dependence of σ_{xy} on the Néel vector space is similar to that of the Berry curvature multipoles on k -space [65] and the spin magnetization multipoles on real space [66].

The quantum origin of the large AHC lies in the SOC-induced avoided crossings, which act as opposite poles of Berry curvature (see Sec. VI of SM [48]). The highest σ_{xy} is achieved if the Fermi energy lies in the middle of the poles. In the case of the antiferromagnetic MnSe bilayer, with the translation of one layer relative to the other by $\frac{1}{3}\mathbf{a} + \frac{1}{3}\mathbf{b}$, we obtain effects similar to those in the d -MnPSe₃ bilayer, including altermagnetism (see Sec. VII of SM [48]). Note that bilayer stacking of AFMs may also lead to weak ferromagnetism [67, 68] where the opposite spin sublattices are not connected by any symmetry. For instance, the polar stacking of bilayer MnSe with basal plane translated by $\frac{1}{3}\mathbf{a} + \frac{2}{3}\mathbf{b}$ leads to weak ferromagnetism in the structure. In such cases, the anomalous Hall response is FM-like, where the AHE is also observed in the plane perpendicular to Néel vector. The weakly FM bilayer MnSe shows σ_{xy} when the Néel vector points along the z -direction similar to conventional FMs [69, 70] (see Sec. VIII of SM [48]) and differ from the AHE in 2D

AMs.

IV. SUMMARY

We have established the principles for obtaining the AHE in 2D AMs. Our analysis shows that TC_2^z and C_2^x are the most common magnetic point group symmetries that suppress the AHE in 2D AMs. Although the AHE is a relativistic effect, spin group symmetries are effective in explaining the unconventional periodicity in the in-plane anomalous Hall response, which can be used to detect the altermagnetic order and Néel vector reversal. We also show that the AHE is forbidden for the g -wave 2D AMs. Our symmetry predictions are supported by first-principles DFT simulations for bilayer MnPSe₃ with two-different layer-stacking geometries used as prototypical candidates for the d - and i -wave AMs. Overall, 2D AMs are promising for the miniaturization of spintronic memory devices, with the Néel vector serving as the write-in mechanism and in-plane AHE for read-off of the information. For the purpose of application in spintronics, 2D AMs that have an in-plane easy axis of magnetization will form a suitable choice. The spin-momentum coupling, and hence, the altermagnetic order can be controlled in twisted magnetic bilayers, depending on the symmetry of the constituent monolayers [24], providing an exceptional platform to achieve the AHE in experiments. Additionally, external parameters such as electric fields or strain may induce AHE in otherwise forbidden AMs [71]. The approach provided here can be extended to other similar transverse effects, such as the anomalous Nernst effect [72] and the nonlinear Hall effect [73]. We anticipate that the theoretical findings of this work will enrich the field of altermagnetic spintronics [4].

ACKNOWLEDGMENTS

This material is based upon work supported by the Air Force Office of Scientific Research under award number FA9550-23-1-0679 and the National Science Foundation Grant No. DMR-1752840. This work used the Expanse cluster at SDSC through allocation PHY180014 from the Advanced Cyberinfrastructure Coordination Ecosystem: Services & Support (ACCESS) program, which is supported by National Science Foundation Grants Nos. 2138259, 2138286, 2138307, 2137603, and 2138296, and Maryland Advanced Research Computing Center.

[1] L.-D. Yuan, Z. Wang, J.-W. Luo, and A. Zunger, Prediction of low- z collinear and noncollinear antiferromagnetic compounds having momentum-dependent spin splitting even without spin-orbit coupling, *Physical Review Materials* **5**, 014409 (2021).

[2] L.-D. Yuan, Z. Wang, J.-W. Luo, and A. Zunger, Strong influence of nonmagnetic ligands on the momentum-dependent spin splitting in antiferromagnets, *Physical Review B* **103**, 224410 (2021).

[3] L. Šmejkal, J. Sinova, and T. Jungwirth, Beyond conventional ferromagnetism and antiferromagnetism: A phase

- with nonrelativistic spin and crystal rotation symmetry, *Physical Review X* **12**, 031042 (2022).
- [4] L. Šmejkal, J. Sinova, and T. Jungwirth, Emerging research landscape of altermagnetism, *Physical Review X* **12**, 040501 (2022).
- [5] S. Hayami, Y. Yanagi, and H. Kusunose, Bottom-up design of spin-split and reshaped electronic band structures in antiferromagnets without spin-orbit coupling: Procedure on the basis of augmented multipoles, *Physical Review B* **102**, 144441 (2020).
- [6] I. Žutić, J. Fabian, and S. D. Sarma, Spintronics: Fundamentals and applications, *Reviews of modern physics* **76**, 323 (2004).
- [7] E. Y. Tsymbal and I. Žutić, *Spintronics Handbook: Spin Transport and Magnetism: Volume Two: Semiconductor Spintronics* (CRC Press, 2019).
- [8] P. Němec, M. Fiebig, T. Kampfrath, and A. V. Kimel, Antiferromagnetic opto-spintronics, *Nature Physics* **14**, 229 (2018).
- [9] J. Železný, P. Wadley, K. Olejník, A. Hoffmann, and H. Ohno, Spin transport and spin torque in antiferromagnetic devices, *Nature Physics* **14**, 220 (2018).
- [10] S. Lee, S. Lee, S. Jung, J. Jung, D. Kim, Y. Lee, B. Seok, J. Kim, B. G. Park, L. Šmejkal, *et al.*, Broken kramers degeneracy in altermagnetic mnte, *Physical Review Letters* **132**, 036702 (2024).
- [11] J. Krempaský, L. Šmejkal, S. D'souza, M. Hajlaoui, G. Springholz, K. Uhlířová, F. Alarab, P. Constantinou, V. Strocov, D. Usanov, *et al.*, Altermagnetic lifting of kramers spin degeneracy, *Nature* **626**, 517 (2024).
- [12] H. Bai, Y. Zhang, Y. Zhou, P. Chen, C. Wan, L. Han, W. Zhu, S. Liang, Y. Su, X. Han, *et al.*, Efficient spin-to-charge conversion via altermagnetic spin splitting effect in antiferromagnet ruo 2, *Physical review letters* **130**, 216701 (2023).
- [13] C.-T. Liao, Y.-C. Wang, Y.-C. Tien, S.-Y. Huang, and D. Qu, Separation of inverse altermagnetic spin-splitting effect from inverse spin hall effect in ruo 2, *Physical Review Letters* **133**, 056701 (2024).
- [14] L. Šmejkal, A. H. MacDonald, J. Sinova, S. Nakatsuji, and T. Jungwirth, Anomalous hall antiferromagnets, *Nature Reviews Materials* **7**, 482 (2022).
- [15] R. Gonzalez Betancourt, J. Zubáč, R. Gonzalez-Hernandez, K. Geishendorf, Z. Šobáň, G. Springholz, K. Olejník, L. Šmejkal, J. Sinova, T. Jungwirth, *et al.*, Spontaneous anomalous hall effect arising from an unconventional compensated magnetic phase in a semiconductor, *Physical Review Letters* **130**, 036702 (2023).
- [16] H. Reichlova, R. Lopes Seeger, R. González-Hernández, I. Kounta, R. Schlitz, D. Kriegner, P. Ritzinger, M. Lammel, M. Leiviskä, A. Birk Hellenes, *et al.*, Observation of a spontaneous anomalous hall response in the mn₅si₃ d-wave altermagnet candidate, *Nature Communications* **15**, 4961 (2024).
- [17] S. Reimers, L. Odenbreit, L. Šmejkal, V. N. Strocov, P. Constantinou, A. B. Hellenes, R. Jaeschke Ubierno, W. H. Campos, V. K. Bharadwaj, A. Chakraborty, *et al.*, Direct observation of altermagnetic band splitting in crsb thin films, *Nature Communications* **15**, 2116 (2024).
- [18] B. Pan, P. Zhou, P. Lyu, H. Xiao, X. Yang, and L. Sun, General stacking theory for altermagnetism in bilayer systems, *Physical Review Letters* **133**, 166701 (2024).
- [19] S. Zeng and Y.-J. Zhao, Description of two-dimensional altermagnetism: Categorization using spin group theory, *Physical Review B* **110**, 054406 (2024).
- [20] S. Zeng and Y.-J. Zhao, Bilayer stacking a-type altermagnet: A general approach to generating two-dimensional altermagnetism, *Physical Review B* **110**, 174410 (2024).
- [21] R. He, D. Wang, N. Luo, J. Zeng, K.-Q. Chen, and L.-M. Tang, Nonrelativistic spin-momentum coupling in antiferromagnetic twisted bilayers, *Physical Review Letters* **130**, 046401 (2023).
- [22] J. Sødequist and T. Olsen, Two-dimensional altermagnets from high throughput computational screening: Symmetry requirements, chiral magnons, and spin-orbit effects, *Applied Physics Letters* **124** (2024).
- [23] M. Milivojević, M. Orozović, S. Picozzi, M. Gmitra, and S. Stavrić, Interplay of altermagnetism and weak ferromagnetism in two-dimensional ruf₄, *2D Materials* **11**, 035025 (2024).
- [24] Y. Liu, J. Yu, and C.-C. Liu, Twisted magnetic van der waals bilayers: An ideal platform for altermagnetism, *Physical Review Letters* **133**, 206702 (2024).
- [25] S. Sheoran and S. Bhattacharya, Nonrelativistic spin splittings and altermagnetism in twisted bilayers of centrosymmetric antiferromagnets, *Physical Review Materials* **8**, L051401 (2024).
- [26] S. Onoda, N. Sugimoto, and N. Nagaosa, Intrinsic versus extrinsic anomalous hall effect in ferromagnets, *Physical review letters* **97**, 126602 (2006).
- [27] R. Shindou and N. Nagaosa, Orbital ferromagnetism and anomalous hall effect in antiferromagnets on the distorted fcc lattice, *Physical review letters* **87**, 116801 (2001).
- [28] K. Kluczyk, K. Gas, M. Grzybowski, P. Skupiński, M. Borysiewicz, T. Fas, J. Suffczyński, J. Domagala, K. Grasa, A. Mycielski, *et al.*, Coexistence of anomalous hall effect and weak magnetization in a nominally collinear antiferromagnet mnte, *Physical Review B* **110**, 155201 (2024).
- [29] M. Leiviskä, J. Rial, A. Bad'ura, R. L. Seeger, I. Kounta, S. Beckert, D. Kriegner, I. Joumard, E. Schmoranzzerová, J. Sinova, *et al.*, Anisotropy of the anomalous hall effect in thin films of the altermagnet candidate mn₅si₃, *Physical Review B* **109**, 224430 (2024).
- [30] G. Kresse and D. Joubert, From ultrasoft pseudopotentials to the projector augmented-wave method, *Physical review b* **59**, 1758 (1999).
- [31] G. Kresse and J. Furthmüller, Efficient iterative schemes for ab initio total-energy calculations using a plane-wave basis set, *Physical review B* **54**, 11169 (1996).
- [32] J. P. Perdew, K. Burke, and M. Ernzerhof, Generalized gradient approximation made simple, *Physical review letters* **77**, 3865 (1996).
- [33] K. Liu, X. Ma, S. Xu, Y. Li, and M. Zhao, Tunable sliding ferroelectricity and magnetoelectric coupling in two-dimensional multiferroic mnse materials, *npj Computational Materials* **9**, 16 (2023).
- [34] M. Rybak, P. E. Faria Junior, T. Woźniak, P. Scharoch, J. Fabian, and M. Birowska, Magneto-optical anisotropies of two-dimensional antiferromagnetic mpx 3 from first principles, *Physical Review B* **109**, 054426 (2024).
- [35] S. L. Dudarev, G. A. Botton, S. Y. Savrasov, C. Humphreys, and A. P. Sutton, Electron-energy-loss spectra and the structural stability of nickel oxide: An lsd+ u study, *Physical Review B* **57**, 1505 (1998).

- [36] S. Grimme, Semiempirical gga-type density functional constructed with a long-range dispersion correction, *Journal of computational chemistry* **27**, 1787 (2006).
- [37] N. Nagaosa, J. Sinova, S. Onoda, A. H. MacDonald, and N. P. Ong, Anomalous hall effect, *Reviews of modern physics* **82**, 1539 (2010).
- [38] A. A. Mostofi, J. R. Yates, Y.-S. Lee, I. Souza, D. Vanderbilt, and N. Marzari, wannier90: A tool for obtaining maximally-localised wannier functions, *Computer physics communications* **178**, 685 (2008).
- [39] S. S. Tsirkin, High performance wannier interpolation of berry curvature and related quantities with wannierberri code, *npj Computational Materials* **7**, 33 (2021).
- [40] M. S. Dresselhaus, G. Dresselhaus, and A. Jorio, *Group theory: application to the physics of condensed matter* (Springer Science & Business Media, 2007).
- [41] H. T. Stokes and D. M. Hatch, Findsym: program for identifying the space-group symmetry of a crystal, *Journal of Applied Crystallography* **38**, 237 (2005).
- [42] M. I. Aroyo, J. M. Perez-Mato, C. Capillas, E. Kroumova, S. Ivantchev, G. Madariaga, A. Kirov, and H. Wondratschek, Bilbao crystallographic server: I. databases and crystallographic computing programs, *Zeitschrift für Kristallographie-Crystalline Materials* **221**, 15 (2006).
- [43] S. V. Gallego, J. M. Perez-Mato, L. Elcoro, E. S. Tasci, R. M. Hanson, K. Momma, M. I. Aroyo, and G. Madariaga, Magdata: towards a database of magnetic structures. i. the commensurate case, *Journal of Applied Crystallography* **49**, 1750 (2016).
- [44] A. Smolyanyuk, L. Šmejkal, and I. I. Mazin, Codebase release r1.0 for amcheck, *SciPost Physics Codebases*, 030 (2024).
- [45] D. B. Litvin and W. Opechowski, Spin groups, *Physica* **76**, 538 (1974).
- [46] Y. Jiang, Z. Song, T. Zhu, Z. Fang, H. Weng, Z.-X. Liu, J. Yang, and C. Fang, Enumeration of spin-space groups: Toward a complete description of symmetries of magnetic orders, *Physical Review X* **14**, 031039 (2024).
- [47] P. Liu, J. Li, J. Han, X. Wan, and Q. Liu, Spin-group symmetry in magnetic materials with negligible spin-orbit coupling, *Physical Review X* **12**, 021016 (2022).
- [48] See Supplemental Material at [link to be inserted by publisher] for further discussion on 2D altermagnetism, symmetry constraints on AHE, AHE–Néel vector relationship, monolayer and bilayer MnPSe₃ and MnSe, which also includes Refs. [3, 33, 69, 74–81].
- [49] T. Jungwirth, X. Marti, P. Wadley, and J. Wunderlich, Antiferromagnetic spintronics, *Nature nanotechnology* **11**, 231 (2016).
- [50] H.-Y. Ma, M. Hu, N. Li, J. Liu, W. Yao, J.-F. Jia, and J. Liu, Multifunctional antiferromagnetic materials with giant piezomagnetism and noncollinear spin current, *Nature communications* **12**, 2846 (2021).
- [51] X. Chen, D. Wang, L. Li, and B. Sanyal, Giant spin-splitting and tunable spin-momentum locked transport in room temperature collinear antiferromagnetic semimetallic monolayer, *Applied Physics Letters* **123** (2023).
- [52] Z. Ni, A. Haglund, H. Wang, B. Xu, C. Bernhard, D. Mandrus, X. Qian, E. Mele, C. Kane, and L. Wu, Imaging the néel vector switching in the monolayer antiferromagnet mnpse3 with strain-controlled ising order, *Nature nanotechnology* **16**, 782 (2021).
- [53] X. Li, X. Wu, and J. Yang, Half-metallicity in mnpse3 exfoliated nanosheet with carrier doping, *Journal of the American Chemical Society* **136**, 11065 (2014).
- [54] N. Sivadas, M. W. Daniels, R. H. Swendsen, S. Okamoto, and D. Xiao, Magnetic ground state of semiconducting transition-metal trichalcogenide monolayers, *Physical Review B* **91**, 235425 (2015).
- [55] M. Aapro, M. N. Huda, J. Karthikeyan, S. Kezilebieke, S. C. Ganguli, H. G. Herrero, X. Huang, P. Liljeroth, and H.-P. Komsa, Synthesis and properties of monolayer mnse with unusual atomic structure and antiferromagnetic ordering, *ACS nano* **15**, 13794 (2021).
- [56] J. Wang, H. Zeng, W. Duan, and H. Huang, Intrinsic nonlinear hall detection of the néel vector for two-dimensional antiferromagnetic spintronics, *Physical Review Letters* **131**, 056401 (2023).
- [57] S. Sheoran and S. Bhattacharya, Multiple zeeman-type hidden spin splittings in pt-symmetric layered antiferromagnets, *Physical Review B* **109**, L020404 (2024).
- [58] X. Yi, Q. Chen, K. Wang, Y. Yu, Y. Yan, X. Jiang, C. Yan, and S. Wang, Exploring the interfacial coupling between graphene and the antiferromagnetic insulator mnpse3, *Physical Review B* **108**, 125427 (2023).
- [59] L. D. Landau, J. S. Bell, M. Kearsley, L. Pitaevskii, E. Lifshitz, and J. Sykes, *Electrodynamics of continuous media*, Vol. 8 (elsevier, 2013).
- [60] L. C. L. Y. Voon and M. Willatzen, *The kp method: electronic properties of semiconductors* (Springer Science & Business Media, 2009).
- [61] R.-C. Xiao, H. Li, H. Han, W. Gan, M. Yang, D.-F. Shao, S.-H. Zhang, Y. Gao, M. Tian, and J. Zhou, Anomalous-hall neel textures in altermagnetic materials, *arXiv preprint arXiv:2411.10147* (2024).
- [62] L.-D. Yuan, A. B. Georgescu, and J. M. Rondinelli, Nonrelativistic spin splitting at the brillouin zone center in compensated magnets, *Physical review letters* **133**, 216701 (2024).
- [63] J. Li, Y. Li, S. Du, Z. Wang, B.-L. Gu, S.-C. Zhang, K. He, W. Duan, and Y. Xu, Intrinsic magnetic topological insulators in van der waals layered mnbi2te4-family materials, *Science Advances* **5**, eaaw5685 (2019).
- [64] L. Webster and J.-A. Yan, Strain-tunable magnetic anisotropy in monolayer crcl3, crbr3, and cri3, *Physical Review B* **98**, 144411 (2018).
- [65] C.-P. Zhang, X.-J. Gao, Y.-M. Xie, H. C. Po, and K. T. Law, Higher-order nonlinear anomalous hall effects induced by berry curvature multipoles, *Physical Review B* **107**, 115142 (2023).
- [66] S. Bhowal and N. A. Spaldin, Ferroically ordered magnetic octupoles in d-wave altermagnets, *Physical Review X* **14**, 011019 (2024).
- [67] D. Jo, D. Go, Y. Mokrousov, P. M. Oppeneer, S.-W. Cheong, and H.-W. Lee, Weak ferromagnetism in altermagnets from alternating *g*-tensor anisotropy, *arXiv preprint arXiv:2410.17386* (2024).
- [68] M. Roig, Y. Yu, R. C. Ekman, A. Kreisel, B. M. Andersen, and D. F. Agterberg, Quasi-symmetry constrained spin ferromagnetism in altermagnets, *arXiv preprint arXiv:2412.09338* (2024).
- [69] T. Cao, D.-F. Shao, K. Huang, G. Gurung, and E. Y. Tsymlal, Switchable anomalous hall effects in polar-stacked 2d antiferromagnet mnbi2te4, *Nano Letters* **23**, 3781 (2023).
- [70] S. K. Chong, Y. Cheng, H. Man, S. H. Lee, Y. Wang, B. Dai, M. Tanabe, T.-H. Yang, Z. Mao, K. A. Moler, *et al.*, Intrinsic exchange biased anomalous hall effect

- in an uncompensated antiferromagnet mnbi_2te_4 , *Nature communications* **15**, 2881 (2024).
- [71] M. Lejman, C. Paillard, V. Juvé, G. Vaudel, N. Guiblin, L. Bellaiche, M. Viret, V. E. Gusev, B. Dkhil, and P. Ruello, Magnetoelastic and magnetoelectric couplings across the antiferromagnetic transition in multiferroic bifeo_3 , *Physical Review B* **99**, 104103 (2019).
- [72] M. Mizuguchi and S. Nakatsuji, Energy-harvesting materials based on the anomalous nernst effect, *Science and technology of advanced materials* **20**, 262 (2019).
- [73] Z. Du, H.-Z. Lu, and X. Xie, Nonlinear hall effects, *Nature Reviews Physics* **3**, 744 (2021).
- [74] C. Wang, Y. Gao, and D. Xiao, Intrinsic nonlinear hall effect in antiferromagnetic tetragonal cumnas , *Physical Review Letters* **127**, 277201 (2021).
- [75] N. Sivadas, S. Okamoto, and D. Xiao, Gate-controllable magneto-optic kerr effect in layered collinear antiferromagnets, *Physical Review Letters* **117**, 267203 (2016).
- [76] U. Herath, P. Tavazde, X. He, E. Bousquet, S. Singh, F. Muñoz, and A. H. Romero, Pyprocar: A python library for electronic structure pre/post-processing, *Computer Physics Communications* **251**, 107080 (2020).
- [77] S. Singh and A. Garcia-Castro, Kagome kmn_3sb_5 metal: Magnetism, lattice dynamics, and anomalous hall conductivity, *Physical Review B* **108**, 245143 (2023).
- [78] H. Chen, Q. Niu, and A. H. MacDonald, Anomalous hall effect arising from noncollinear antiferromagnetism, *Physical review letters* **112**, 017205 (2014).
- [79] L. Šmejkal, R. González-Hernández, T. Jungwirth, and J. Sinova, Crystal time-reversal symmetry breaking and spontaneous hall effect in collinear antiferromagnets, *Science advances* **6**, eaaz8809 (2020).
- [80] R. Peng, T. Zhang, Z. He, Q. Wu, Y. Dai, B. Huang, and Y. Ma, Intrinsic layer-polarized anomalous hall effect in bilayer $\text{mn bi}_2\text{te}_4$, *Physical Review B* **107**, 085411 (2023).
- [81] A. Gao, Y.-F. Liu, C. Hu, J.-X. Qiu, C. Tzschaschel, B. Ghosh, S.-C. Ho, D. Bérubé, R. Chen, H. Sun, *et al.*, Layer hall effect in a 2d topological axion antiferromagnet, *Nature* **595**, 521 (2021).

Supplemental Material for “Spontaneous Anomalous Hall Effect in Two-Dimensional Altermagnets”

Sajjan Sheoran and Pratibha Dev
Department of Physics and Astronomy, Howard University, Washington D.C., USA

- I. 2D altermagnetism: group theoretic considerations
- II. Symmetry constraints on AHE
- III. AHE and Néel vector relationship
- IV. Monolayer MnPSe₃ and MnSe
- V. Altermagnetism in bilayer MnPSe₃
- VI. Origin of AHE in bilayer MnPSe₃
- VII. AHE in altermagnetic bilayer MnSe
- VIII. AHE in weakly ferromagnetic bilayer MnSe

I. 2D Altermagnetism: group theoretic considerations

The main text describes symmetry considerations that lead to the emergence of 2D altermagnetism. In this subsection, we provide greater details of how group theoretic considerations were used to obtain our results.

If the Hamiltonian of a system remains invariant under a certain symmetry (O), it transforms the energy eigenstate (E) as $OE(s, \mathbf{k}) = E(s', \mathbf{k}')$, where $s' = Os$ and $\mathbf{k}' = O\mathbf{k}$. In the nonrelativistic case, spin and real space are decoupled. In this case, the symmetry transformation, O , can be written as $O = [O_1||O_2]$, where O_1 and O_2 act only on the spin and real spaces, respectively. Generally, $[O_1||O_2]$ can take one of four forms: $[E||E]$, $[O_1||E]$, $[E||O_2]$, and $[O_1||O_2]$. Here, $[E||E]$ represents the trivial identity in both spaces, $[O_1||E]$ corresponds to spin-only symmetry, $[E||O_2]$ represents crystallographic symmetry (nonmagnetic point group), and $[O_1||O_2]$ represents nontrivial spin group symmetry. Collinear magnets can exhibit spin-only symmetries, such as C_∞ (arbitrary rotation around the collinear spin axis) and \bar{C}_2 (a two-fold rotation around an axis perpendicular to the collinear spin axis, followed by inversion) in addition to the trivial identity. The symmetry C_∞ allows the separation of spin-up and spin-down bands. Meanwhile, spin-space inversion in \bar{C}_2 occurs with the time-reversal operation, which also acts on the real space. As a result, collinear magnets always exhibit $[\bar{C}_2||T]$ symmetry. For collinear magnets without spin-orbit coupling (SOC), the general symmetry operation can be written as:

$$([E||E] + [C_\infty||E] + [\bar{C}_2||T] + [C_\infty||E][\bar{C}_2||T])[O_1||O_2],$$

where the terms inside the first set of brackets represent the spin-only group, and $[O_1||O_2]$ is a nontrivial spin group symmetry dependent on the crystal and magnetic structure. For example, if opposite spin sublattices are connected by inversion (P) or translation (τ), the nontrivial spin group symmetry is $[C_2||P]$ or $[C_2||\tau]$, where C_2 represents a two-fold rotation about an axis perpendicular to the collinear spin axis. The C_2 acts on spin-space same as spin-space inversion [the difference being that it is not accompanied by time-reversal (T)]. The $[\bar{C}_2||T][C_2||P]$ and $[C_2||\tau]$ symmetries transform energy eigenstates as follows:

$$[\bar{C}_2||T][C_2||P]E(s, \mathbf{k}) = [\bar{C}_2||T]E(-s, -\mathbf{k}) = E(-s, \mathbf{k}) \quad (1)$$

$$[C_2||\tau]E(s, \mathbf{k}) = E(-s, \mathbf{k}) \quad (2)$$

Therefore, $[C_2||P]$ and $[C_2||\tau]$ lead to spin degeneracy at arbitrary an \mathbf{k} -point. For the 2D materials, $\mathbf{k} = k_x i + k_y j$ ($k_z = 0$). The transformations of $[C_2||M_z]$ and $[\bar{C}_2||T][C_2||C_{2z}]$ act on energy eigenstates as follows:

$$[C_2||M_z]E(s, \mathbf{k}) = E(-s, \mathbf{k}) \quad (3)$$

$$[\bar{C}_2||T][C_2||C_{2z}]E(s, \mathbf{k}) = [\bar{C}_2||T]E(-s, -\mathbf{k}) = E(-s, \mathbf{k}) \quad (4)$$

Here, the operator M_z represents mirror symmetry about the $z = 0$ plane, while C_{2z} denotes a two-fold rotation about the z -axis in real space. Consequently, the symmetries $[C_2||C_{2z}]$ and $[C_2||M_z]$ enforce spin degeneracy in 2D materials. To break spin degeneracy in 2D materials, opposite spin sublattices must not be related by P , τ , M_z , or C_{2z} .

For 2D altermagnetism to emerge, there must be specific symmetries that connect opposite spin sublattices. While, in principle, any symmetry except P , τ , M_z , and C_{2z} can connect opposite spin sublattices, not all such symmetries are practical in 2D materials. For example, 2D materials cannot exhibit C_3^x symmetry. Similarly, although C_3^z symmetry is allowed in 2D materials, it cannot connect opposite spin sublattices, as it would lead to $[C_2||C_3^z][C_2||C_3^z][C_2||C_3^z] = [C_2||E]$, which means opposite spin sublattices are connected by identity (not possible for magnets). Similarly it can be shown that the only symmetries that can connect opposite spin sublattices in 2D materials are C_2^x , C_4^z , and M_x . In spin group notation, the corresponding symmetries are $[C_2||C_2^x]$, $[C_2||C_4^z]$, and $[C_2||M_x]$. It is worth mentioning that symmetry $[C_2||S_4^z]$ may also connect opposite spin sublattices, however, it is redundant as it can be written as combination of $[E||P]$ and $[C_2||C_4^z]$ and we are concerned only about generators.

II. Symmetry constraints on AHE

In what follows, we provide our procedure for determining the constraints on the AHC tensor components, which are imposed by unitary and antiunitary symmetry operations (see Table I of the main text). The AHC is expressed as:

$$\sigma_{\alpha\beta} = -\epsilon_{\alpha\beta\gamma} \frac{e^2}{\hbar} \int \frac{d\mathbf{k}}{(2\pi)^3} \sum_n f(\mathcal{E}_{n,\mathbf{k}}) \Omega_\gamma(n, \mathbf{k}), \quad (5)$$

where $\Omega_\gamma(n, \mathbf{k})$ is the Berry curvature of band n at the \mathbf{k} -point, $\mathcal{E}_{n,\mathbf{k}}$ is the energy eigenvalue, $\epsilon_{\alpha\beta\gamma}$ is the Levi-Civita symbol, and $f(\mathcal{E}_{n,\mathbf{k}})$ is the Fermi-Dirac distribution function. The Berry curvature and $\boldsymbol{\sigma}_H (= \sigma_{zy}, \sigma_{xz}, \sigma_{yx})$ transform as pseudovectors. Also, the AHC tensor is antisymmetric in nature, $\sigma_{ij} = -\sigma_{ji}$. For example, under T symmetry, $T\sigma_{xy}(\mathbf{k}) = -\sigma_{xy}(-\mathbf{k})$. Therefore, the summation in Eq. 5 evaluates to zero, even though the Berry curvature is not zero at every \mathbf{k} -point. The T symmetry is satisfied for nonmagnetic materials; a well-known example is MoS₂. Similarly, PT symmetry leads to

$$PT\boldsymbol{\Omega}(\mathbf{k}) = -P\boldsymbol{\Omega}(-\mathbf{k}) = -\boldsymbol{\Omega}(\mathbf{k}),$$

which results in zero Berry curvature at every \mathbf{k} -point [$\boldsymbol{\Omega}(\mathbf{k}) = 0$], thereby forbidding the anomalous Hall effect (AHE).

Let us consider the case of M_x symmetry. The M_x symmetry transforms the Berry curvature as

$$M_x\boldsymbol{\Omega}(\mathbf{k}) = (\Omega_x, -\Omega_y, -\Omega_z)(-k_x, k_y, k_z).$$

Consequently, σ_{zy} is the only nonzero component in this case. Alternatively, M_x transforms $\boldsymbol{\sigma}_H$ as $M_x(\sigma_{zy}, \sigma_{xz}, \sigma_{yx}) = (\sigma_{zy}, -\sigma_{xz}, -\sigma_{yx})$, which implies that only $\sigma_{yz} \neq 0$. Using a similar procedure for the rest of the symmetry operations, one can build Table I of the main text.

III. AHE and Néel vector relationship

Figure 4 of the main text shows the functional dependence of the AHE on the Néel vector. Writing the general form of the AHC as $\sigma_{xy} = \sigma_{xy}(\mathbf{N})$, one can obtain the functional dependence of the AHE on the Néel vector as:

$$\sigma_{xy}(\mathbf{N}) = \sum_{m,n,r} \lambda_{mnr} N_x^m N_y^n N_z^r, \quad (6)$$

where, λ_{mnr} are the coefficients that determine the contribution of each term. Some terms are forbidden by symmetry. For example, σ_{xy} cannot be even in \mathbf{N} as it would violate the Onsager reciprocity relation: $\sigma_{xy}(\mathbf{N}) = -\sigma_{xy}(-\mathbf{N})$. The Néel vector is determined by the magnetization of sublattices. Therefore, the Néel vector transforms as a pseudovector under the space group operation, O . However, it acquires an additional sign (\pm), depending on whether transformation exchanges opposite ($-$) or same ($+$) spin sublattices (see Fig. 1 of main text). Mathematically, this can be expressed as:

$$O\mathbf{N} = \pm \text{Det}(O)D(O)\mathbf{N}. \quad (7)$$

where $\text{Det}(O)$ is the determinant of the matrix $[D(O)]$ for the symmetry operation O . For instance, if the opposite spin sublattices are connect by Inversion (P), then $P\mathbf{N} = (-1)(-1)(-I_{3\times 3})\mathbf{N}$ and therefore $P\mathbf{N} = -\mathbf{N}$. Also, P transforms σ_H as $P\sigma_H = (-1)(-I_{3\times 3})\sigma_H$, which mean $P\sigma_{xy} = \sigma_{xy}$. Therefore, when the opposite spin sublattices are connect by inversion, all of the λ_{mnr} coefficients are symmetry forbidden, suppressing the AHE. This can also be understood from the fact that the system has PT ($[C_2||P]$ in spin group notation) symmetry and so linear AHE is not allowed (although, higher-order AHE may be allowed). Similar arguments can be used to show that if inversion symmetry connects the same spin sublattices ($[E||P]$), it does not impose any condition on the Hall effect. These observation are consistent with the Table I of the main text.

For the case of 2D altermagnetism (see Sec I of SM), the allowed spin group symmetries are $[C_2||C_2^x, M_x, C_4^z]$ (which connect opposite spin sublattices) and $[E||E, P, C_2^z, M_z, C_2^x, M_x, C_3^z, C_4^z]$ (which connect same-spin sublattices). Note that the in-plane direction is chosen along the x -axis. Other symmetry operations, such as $[C_2||S_4^z]$, $[E||S_4^z]$, and $[E||S_3^z]$ can be generated from the aforementioned operations, and thus are safely ignored.

Out of 80 layer groups only a few can have spin group symmetry $[C_2||C_2^x, M_x, C_4^z]$. The possible layer groups are $2/m$, mmm , $4/m$, $4/mmm$, $3m$, and $6/mmm$. Note that layer groups containing screw axes and glide planes are ignored, although they can also be included. For example, observations for $2/m$ should also apply to $2_1/m$, $2/b$, and $2_1/b$. For a particular layer group, symmetry operations will either connect opposite spin sublattices or same-spin sublattices. Operations connecting same- and opposite-spin sublattices are highlighted with superscripts, 1 and 2, respectively, which are added before the symmetry operation. For example, in ${}^{24/1}m^2m^1m$, the fourfold rotation connects opposite spin sublattices, the horizontal mirror connects same-spin sublattices, and the two vertical mirror planes connect opposite spin sublattices. There can be seven nontrivial spin layer groups, namely ${}^{22/2}m$, ${}^2m^2m^1m$, ${}^{24/1}m$, ${}^{24/1}m^2m^1m$, ${}^{24/1}m^2m^2m$, ${}^{1\bar{3}}2m$, and ${}^{16/1}m^2m^2m$. Therefore, we derive the relationship between σ_{xy} and \mathbf{N} for these seven nontrivial spin layer groups in Table II of the main text. Here, we highlight the case of ${}^{24/1}m^2m^1m$ (see Table S1). The generators of ${}^{24/1}m^2m^1m$ are $[E||E]$, $[E||P]$, $[E||C_2^z]$, $[E||C_2^x]$, and $[C_2||C_4^z]$. The invariant common to all symmetry operations is $N_x^2N_z - N_y^2N_z$. Therefore, for the ${}^{24/1}m^2m^1m$ nontrivial spin layer group, we obtain

$$\sigma_{xy}^{24/1m^2m^1m} = \lambda_{201}(N_x^2N_z - N_y^2N_z).$$

TABLE S1: Summary of invariants under the symmetry operations of ${}^{24/1}m^2m^1m$.

Symmetry Operation	Constraint on $\sigma_{xy}(N_x, N_y, N_z)$	Symmetry Invariants
$[E E]$	$\sigma_{xy}(N_x, N_y, N_z) = \sigma_{xy}(N_x, N_y, N_z)$	$N_x^m N_y^n N_z^r (m + n + r = \text{odd})$
$[E P]$	$\sigma_{xy}(N_x, N_y, N_z) = \sigma_{xy}(N_x, N_y, N_z)$	$N_x^m N_y^n N_z^r (m + n + r = \text{odd})$
$[C_2 C_4^z]$	$\sigma_{xy}(N_x, N_y, N_z) = \sigma_{xy}(-N_y, N_x, -N_z)$	$N_x^2 N_z - N_y^2 N_z$
$[E C_2^z]$	$\sigma_{xy}(N_x, N_y, N_z) = \sigma_{xy}(-N_x, -N_y, N_z)$	$N_z, N_x^2 N_z, N_y^2 N_z$
$[E C_2^x]$	$\sigma_{xy}(N_x, N_y, N_z) = -\sigma_{xy}(N_x, -N_y, -N_z) = \sigma_{xy}(-N_x, N_y, N_z)$	$N_y, N_z, N_x^2 N_y, N_x^2 N_z, N_y^2 N_z, N_y N_z^2$

IV. Monolayer MnPSe₃ and MnSe

The opposite spin sublattices in monolayer MnPSe₃ and MnSe are connected by $[C_2||P]$ symmetry. Therefore, the bands are degenerate throughout the BZ (see Fig. S1). Similarly, the bands remain degenerate throughout the BZ with the inclusion of SOC due to PT symmetry (see Sec. I). PT symmetry also suppresses the AHE in both cases (see Sec. II). Note that we have chosen these two materials as they exhibit tilted Dirac cones near the valence band maximum along the $\Gamma - M$ path. These tilted Dirac cones may act as a source of strong Berry curvature when PT symmetry is broken (see, for example, Ref. [1]).

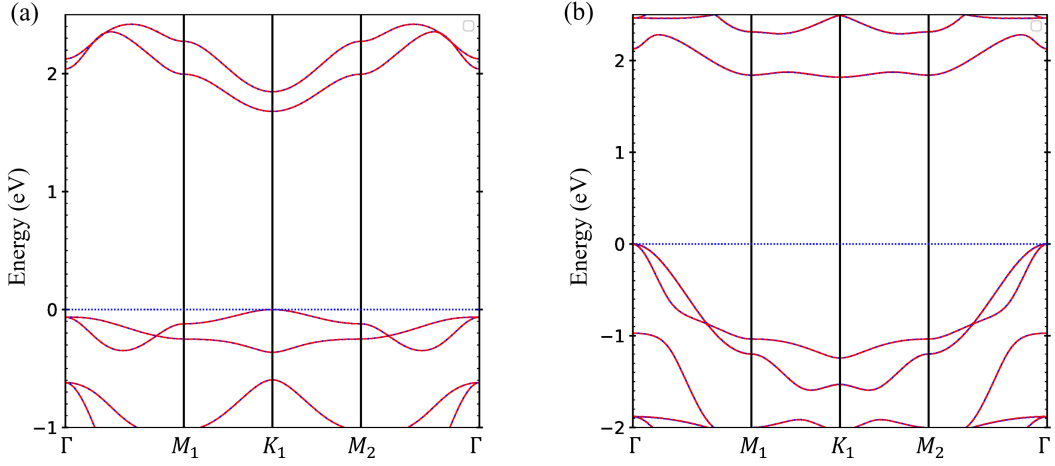


Fig. S1: Spin-polarized band structure of (a) monolayer MnPSe_3 and (b) monolayer MnSe without SOC. The red and blue curves denote the spin-up and spin-down bands, respectively. The bands are degenerate throughout the BZ due to spin group symmetry $[C_2||P]$. Similarly, the bands remain degenerate throughout the BZ with the inclusion of SOC due to PT symmetry (not shown here; see, for example, Refs. [2, 3]). We make use of PyProcar [4] to plot the band structures.

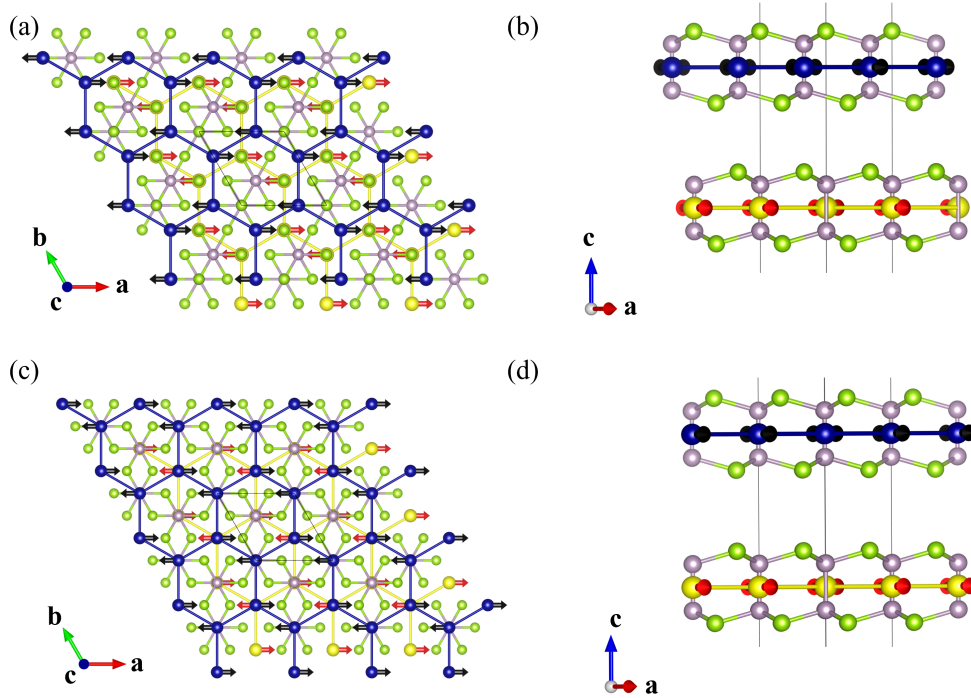


Fig. S2: The top and side views of bilayer $d\text{-MnPSe}_3$ [(a) and (b)] and $i\text{-MnPSe}_3$ [(c) and (d)]. The blue and yellow spheres denote the Mn atoms from the top and bottom layers, respectively. The green and grey spheres represent P and Se atoms, respectively.

V. Altermagnetism in bilayer MnPSe_3

Figure S2 shows the two possible high symmetry stackings of bilayer MnPSe_3 , named $d\text{-MnPSe}_3$ and $i\text{-MnPSe}_3$. To understand the altermagnetism in bilayer MnPSe_3 , we plot constant energy surfaces for $d\text{-MnPSe}_3$ and $i\text{-MnPSe}_3$ in Fig. S3. The $d\text{-MnPSe}_3$ and $i\text{-MnPSe}_3$ exhibit 2 and 6 spin-degenerate nodal lines passing through the Γ point, respectively. For $d\text{-MnPSe}_3$, this can be understood from the fact that $d\text{-MnPSe}_3$ has $[C_2||M_{-\sqrt{3}x+y}]$ symmetry,

which enforces spin degeneracy along the Γ - K_1 path. The $[\overline{C}_2||T][C_2||M_{-\sqrt{3}x+y}]$ symmetry enforces spin degeneracy along the other spin-degenerate line. In a similar way, six spin group symmetries for i -MnPSe₃—three being $[C_2||C_2^x]$, $[C_2||C_2^{x+\sqrt{3}y}]$, and $[C_2||C_2^{-x+\sqrt{3}y}]$, and three being their combinations with $[\overline{C}_2||T]$ —enforce spin degeneracy along the Γ - K and Γ - M directions (six in total). The nonrelativistic dispersions in d -MnPSe₃ and i -MnPSe₃ are classified as d -wave and i -wave altermagnetism, respectively. Similarly, g -wave altermagnetism exhibits 4 spin-degenerate nodal lines crossing the Γ point in the 2D Brillouin zone [5].

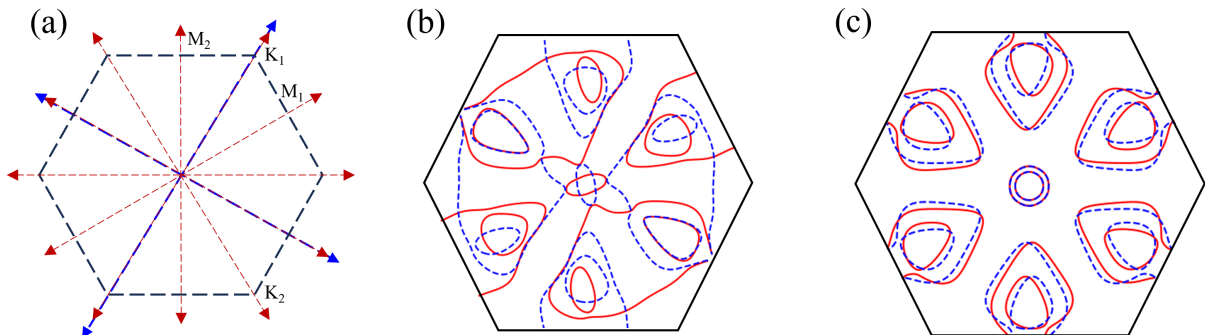


Fig. S3: (a) The Brillouin Zone of the hexagonal unit cell, showing key symmetry points used in the band structure plots. (b) Constant energy contour at -0.23 eV for d -MnPSe₃ and (c) constant energy contour at -0.17 eV for i -MnPSe₃. Red solid lines and blue dashed lines represent spin-up and spin-down bands, respectively. Spin-degenerate nodal lines are highlighted in (a), with blue and red arrows marking the spin-degenerate lines for d -MnPSe₃ and i -MnPSe₃, respectively.

VI. Origin of AHE in bilayer MnPSe₃

The Berry curvature shows peaks at the band anticrossings in FMs [6], AFMs [7], and AMs [8]. It is not surprising then that the contribution to AHC in d -MnPSe₃ and i -MnPSe₃ is highest around their respective band anticrossings (see Fig. S4). Therefore, the 2D materials that feature symmetry-protected Dirac and Weyl points and nodal lines may be used to designed AMs with strong anomalous Hall response.

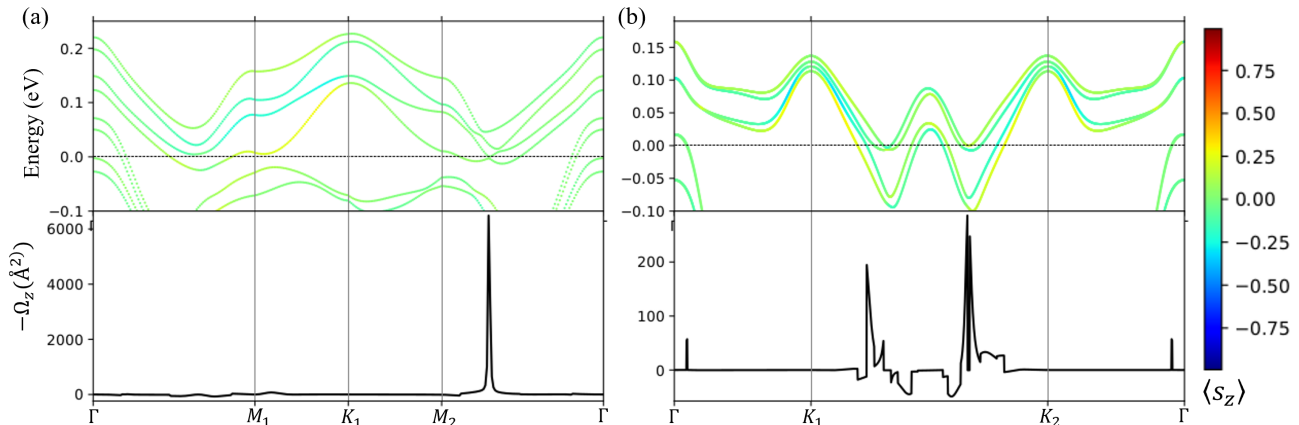


Fig. S4: The spin-polarized band structure (upper panel) and total Berry curvature $-\Omega_z(\mathbf{k})$ (lower panel) for (a) d -MnPSe₃ and (b) i -MnPSe₃ with SOC and magnetization along the x -direction. The spin-polarized bands are colored according to the spin expectation along the z -direction. The Fermi energy is shifted to the energy level at which significant anomalous Hall conductivity is observed, as discussed in the main text (-0.23 eV and -0.17 eV below the valence band maximum for d -MnPSe₃ and i -MnPSe₃, respectively).

VII. AHE in altermagnetic bilayer MnSe

To show that our group theoretic analysis is general and applies to other materials as well, we also performed the calculations on bilayer MnSe. First we obtained the bilayer MnSe by taking the mirror reflection of the lower layer, followed by the in-plane translation of $1/3\mathbf{a} + 1/3\mathbf{b}$. The spin polarized band structure of bilayer MnSe shows the d -wave altermagnetism [see Fig. S5(a)]. The opposite spin sublattices are connected by $C_2^{-\sqrt{3}x+y}$. The altermagnetic bilayer MnSe show anomalous Hall response similar to d -MnPSe₃ [see Fig. S5(b)].

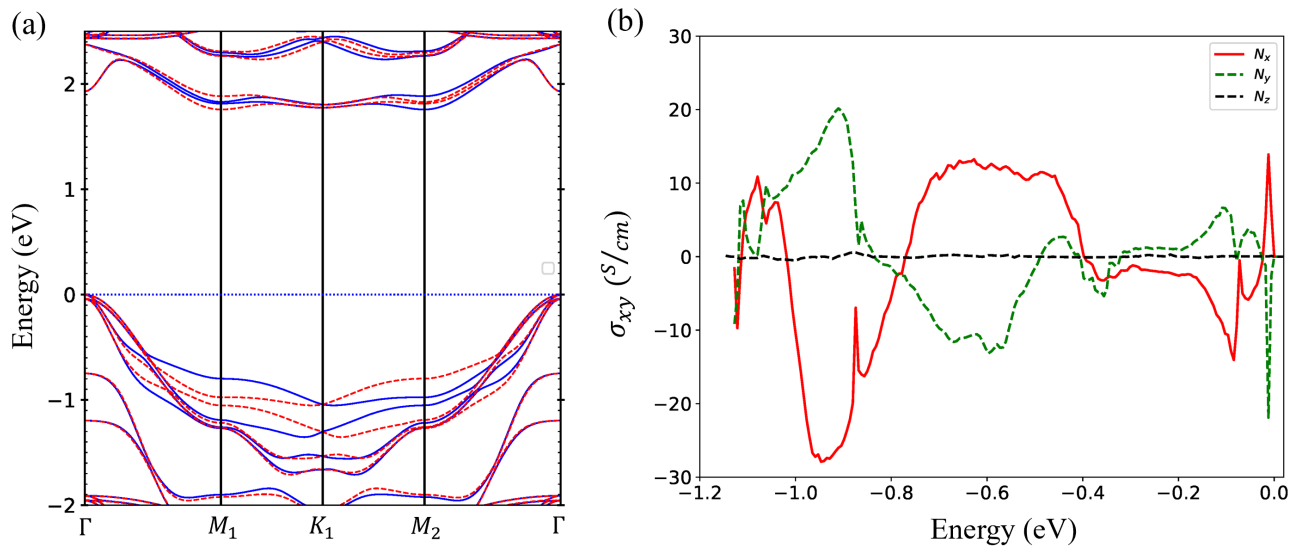


Fig. S5: (a) Spin polarized bands (without SOC) and (b) anomalous Hall conductivity σ_{xy} of altermagnetic bilayer MnSe. The zero Fermi energy corresponds to the valence band maximum.

VIII. AHE in weakly ferromagnetic bilayer MnSe

In this section, we discuss how AHE of an altermagnetic bilayer can be distinguished from the weakly ferromagnetic bilayer. For this, we used the bilayer MnSe obtained using the basal plane translation $1/3\mathbf{a} + 2/3\mathbf{b}$ and $2/3\mathbf{a} + 1/3\mathbf{b}$. Following Ref [3], we name those stacking arrangements as AB-MnSe and BA-MnSe. The sliding ferroelectricity in bilayer MnSe leads to nonzero net magnetic moment (weak ferromagnetism). A recent study [*npj Computational Materials* **9** (16), 2023] highlights the weak ferromagnetism in AB-MnSe and BA-MnSe, which is switchable by inter-layer sliding from AB to BA stacking. We have plotted the bandstructure of AB-MnSe and BA-MnSe in Figs. S6(a) and S6(b). The weak ferromagnetism can be understood from the fact that no crystal symmetry connects opposite spin sublattices in these structures. The weak switchable ferromagnetism is evident from the spin polarized band structure in Figs. S7(a) and S7(b). Next, we obtained the AHC, σ_{xy} , of the weakly ferromagnetic bilayer MnSe for different Néel vector orientations. We observe that this weakly ferromagnetic bilayer MnSe shows FM-like Hall response where, the σ_{xy} is nonzero when the Néel vector points along z -direction. Note that σ_{xy} is reversed not only upon switching the Néel vector from the z to $-z$ direction, but also by changing the stacking from AB to BA. These FM-like Hall responses in bilayer AFMs have recently gained much attention. For example, FM-type Hall responses have been reported for MnBi₂Te₄ through sliding ferroelectricity [9, 10] or external electric field [11]

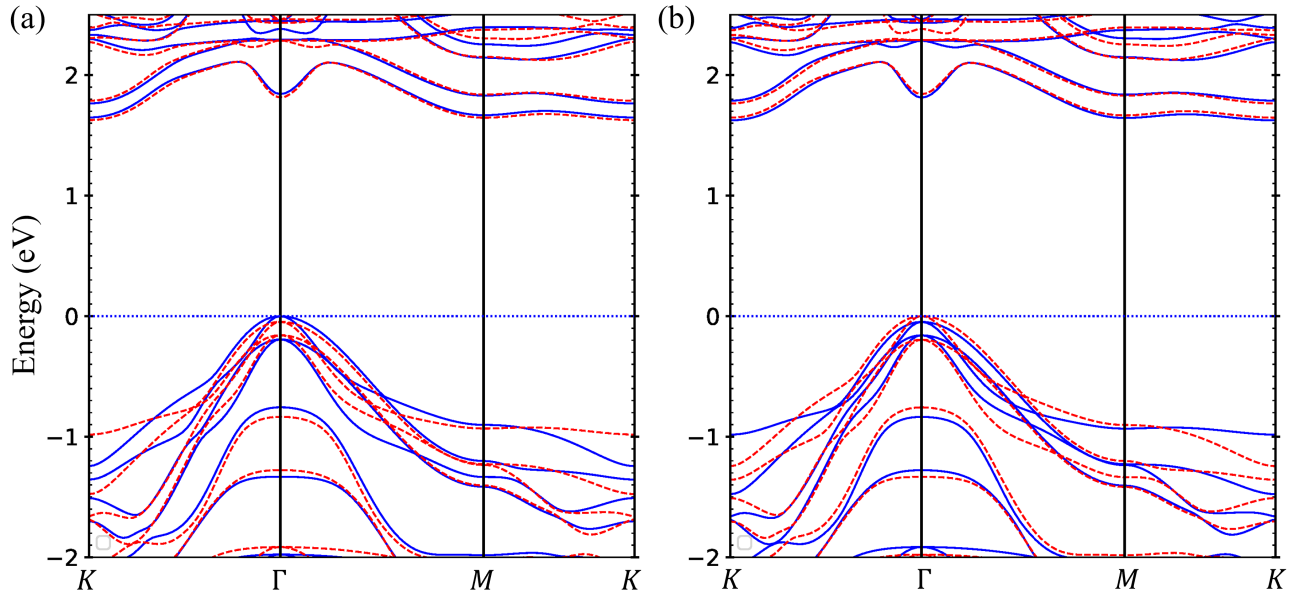


Fig. S6: Spin polarized bands of (a) AB-MnSe and (d) BA-MnSe without SOC. The zero Fermi energy corresponds to the valence band maximum.

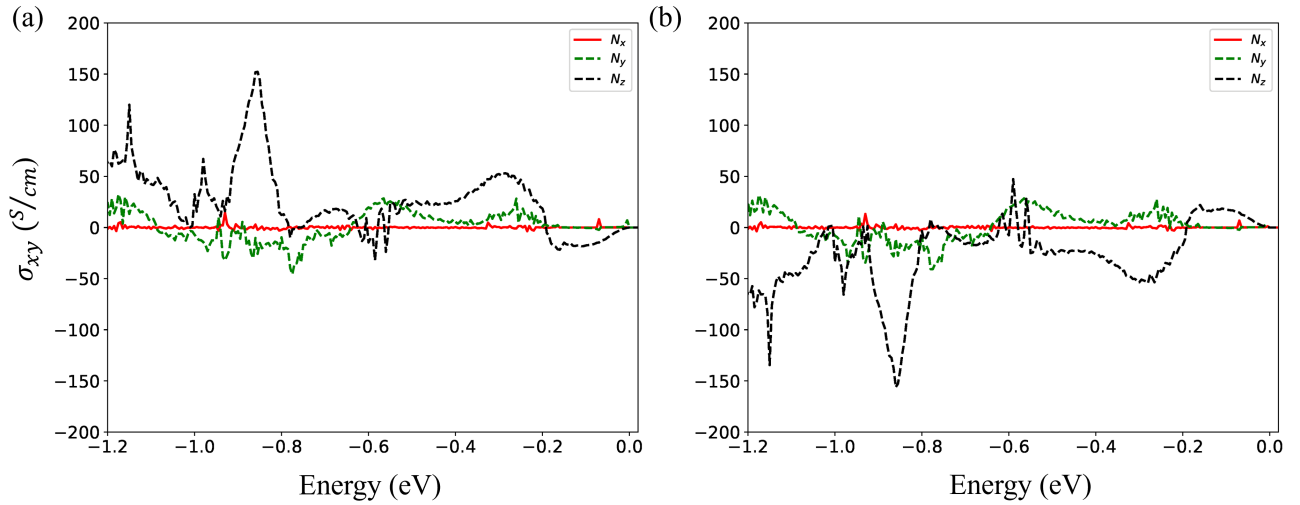


Fig. S7: Anomalous Hall conductivity σ_{xy} of (a) AB-MnSe and (d) BA-MnSe as a function of Fermi energy for different orientations of the Néel vector. The zero Fermi energy corresponds to valence band maximum.

REFERENCES

-
- [1] C. Wang, Y. Gao, and D. Xiao, Intrinsic nonlinear hall effect in antiferromagnetic tetragonal cumnas, *Physical Review Letters* **127**, 277201 (2021).
 - [2] N. Sivadas, S. Okamoto, and D. Xiao, Gate-controllable magneto-optic kerr effect in layered collinear antiferromagnets, *Physical Review Letters* **117**, 267203 (2016).
 - [3] K. Liu, X. Ma, S. Xu, Y. Li, and M. Zhao, Tunable sliding ferroelectricity and magnetoelectric coupling in two-dimensional multiferroic mnse materials, *npj Computational Materials* **9**, 16 (2023).

- [4] U. Herath, P. Tavadze, X. He, E. Bousquet, S. Singh, F. Muñoz, and A. H. Romero, Pyprocar: A python library for electronic structure pre/post-processing, *Computer Physics Communications* **251**, 107080 (2020).
- [5] L. Šmejkal, J. Sinova, and T. Jungwirth, Beyond conventional ferromagnetism and antiferromagnetism: A phase with nonrelativistic spin and crystal rotation symmetry, *Physical Review X* **12**, 031042 (2022).
- [6] S. Singh and A. Garcia-Castro, Kagome kmn 3 sb 5 metal: Magnetism, lattice dynamics, and anomalous hall conductivity, *Physical Review B* **108**, 245143 (2023).
- [7] H. Chen, Q. Niu, and A. H. MacDonald, Anomalous hall effect arising from noncollinear antiferromagnetism, *Physical review letters* **112**, 017205 (2014).
- [8] L. Šmejkal, R. González-Hernández, T. Jungwirth, and J. Sinova, Crystal time-reversal symmetry breaking and spontaneous hall effect in collinear antiferromagnets, *Science advances* **6**, eaaz8809 (2020).
- [9] R. Peng, T. Zhang, Z. He, Q. Wu, Y. Dai, B. Huang, and Y. Ma, Intrinsic layer-polarized anomalous hall effect in bilayer mn bi 2 te 4, *Physical Review B* **107**, 085411 (2023).
- [10] T. Cao, D.-F. Shao, K. Huang, G. Gurung, and E. Y. Tsymbal, Switchable anomalous hall effects in polar-stacked 2d antiferromagnet mnbi2te4, *Nano Letters* **23**, 3781 (2023).
- [11] A. Gao, Y.-F. Liu, C. Hu, J.-X. Qiu, C. Tzschaschel, B. Ghosh, S.-C. Ho, D. Bérubé, R. Chen, H. Sun, *et al.*, Layer hall effect in a 2d topological axion antiferromagnet, *Nature* **595**, 521 (2021).